Comparison of Two Physical Models for Fitting PEM Fuel Cell Impedance Spectra Measured at a Low Air Flow Stoichiometry

Tatyana Reshetenko[a,*] and Andrei Kulikovsky[b,c,*,z]

[a]*Hawaii Natural Energy Institute, University of Hawaii, Honolulu, Hawaii 96822, USA*
[b]*Forschungszentrum Jülich GmbH, Institute of Energy and Climate Research, IEK–3: Electrochemical Process Engineering, D-52425 Jülich, Germany*
[c]*Lomonosov Moscow State University, Research Computing Center, 119991 Moscow, Russia*

Local impedance spectra of a segmented PEM fuel cell operated at an air flow stoichiometry of $\lambda = 2$ are measured. The local spectra are fitted with the recent 1D and quasi–2D (q2D) physical models for PEMFC impedance. The q2D model takes into account oxygen transport in the gas channel, while the 1D model ignores this transport assuming infinite stoichiometry of the air flow. Analysis of the q2D expression for the GDL impedance Z_{gdl}^{∞} at $\lambda \to \infty$ shows that the contribution of Z_{gdl}^{∞} to the total cell impedance rapidly decays with the frequency growth. We derive an equation for the boundary frequency $f_{\rm lim}$, above which this contribution is small. We show that the 1D model can be fitted to the high–frequency part ($f > f_{\rm lim}$) of a spectrum acquired at $\lambda \simeq 2$, ignoring the low–frequency arc due to the oxygen transport in the channel. Comparison of fitting parameters resulted from the 1D and q2D models confirms this idea.

Manuscript submitted August 28, 2015; revised manuscript received November 9, 2015. Published January 2, 2016.

Polymer electrolyte membrane fuel cells (PEMFCs) generate electricity due to splitting the hydrogen–oxygen combustion reaction into two half–reactions producing and consuming charged particles. Understanding transport and kinetic potential losses in these cells is crucial for cell design. Electrochemical impedance spectroscopy (EIS) provides a unique opportunity to separate contributions of different processes into the total potential loss in a cell.[1,2] Deciphering experimental impedance spectra requires modeling though.

The simplest and fastest way to rationalize the spectra is the transmission line modeling (TLM). This approach aims at construction of equivalent electric circuit, which has a spectrum close to the measured one. The circuit is usually assembled out of R, C and L–elements, and out of a number of elements representing classic impedances of electrochemical systems. Two well–known examples are the Warburg element,[3] which describes impedance of a transport layer attached to a planar electrode, and Gerischer element[4] representing impedance of a transport layer with the distributed chemical reaction. The TLM has been widely used in fuel cell studies (see e.g. Refs. 5 and 6); however, validity of this approach cannot be rigorously proved. First, there is no guarantee, that the selected equivalent circuit is unique. Second, the classic solutions for impedance of a system with the planar electrode[3,4] are, in general, not applicable to a porous catalyst layer with the distributed electrochemical reaction.[7,8] In addition, determination of the cell physical transport and kinetic parameters from the equivalent circuit elements is usually beyond the scope of the TLM.

This explains growing interest in physical modeling of PEMFC impedance.[9–22] Generally, a physical impedance model can be obtained from any transient performance model of a cell by making a standard procedure of linearization and Fourier–transform (see e.g. Ref. 23 for mathematical details). The resulting system of linear equations for the perturbation amplitudes is, in general, a complex–valued boundary–value problem (BVP), which can only be solved numerically. At high frequencies of the exciting signal, the solution of the BVP exhibits large spatial gradients, which requires fine numerical meshes and hence quite a significant CPU time. As a result, the least–squares (LS) algorithms employing the physical impedance model appear to be slow for massive spectra processing.

An alternative approach is based on analytical solutions for the PEMFC impedance.[7,23–28] Under certain restricting conditions, the BVP discussed above can be solved analytically yielding explicit expressions for the cell impedance. Typically, these expressions are obtained if the cell current density is sufficiently small. The LS fitting algorithms based on analytical impedances are much faster. Recently, an analytical one–dimensional (1D) physical model for PEMFC impedance[7] has been used for the cell characterization by means of fitting this model to the experimental spectra acquired at a high stoichiometry of the air flow.[29]

Most of the physical impedance models ignore the impedance due to the air flow in the channel. This approach is justified if the air (oxygen) stoichiometry λ of the flow is large. However, in real situations, PEMFCs operate at $\lambda \simeq 2$, and the "channel" impedance could be quite significant.[21,30–32] Recently, an analytical quasi–2D model for impedance of a PEMFC with the straight air channel has been developed.[8] This model includes the effect of the air flow in the channel on the cell impedance. Below, this model will be referred to as the q2D model.

In this work, we use the 1D[7] and the q2D[8] models as the tools for PEMFC characterization at a low stoichiometry of the air flow. We show that with the growth of the frequency of the exciting signal, the impedance due to the air flow in the channel vanishes. We calculate the frequency $f_{\rm lim}$, above which this impedance can be ignored. It follows, that the points with $f > f_{\rm lim}$ of a low–stoichiometry spectrum can be fitted using the 1D model. Next, we fit the 1D and the q2D models to the local experimental spectra of the segmented cell operated at the air flow stoichiometry of $\lambda = 2$. Comparison of fitting parameters resulted from the two models validates the idea of using the 1D model for fitting a part of the spectra with $f > f_{\rm lim}$.

Experimental

The experiments have been performed using Hawaii Natural Energy Institute's (HNEI) segmented cell system.[33] The segmented cell approach used in this study follows the ideas developed in Refs. 34–37. HNEI's system is partially based on the design[34,36] using closed loop Hall sensors (Honeywell CSNN 191) and an improved data acquisition system, which allows us to perform simultaneous measurements of spatial EIS, linear sweep voltammetry and cyclic voltammetry.[33] This diagnostic tool is operated as a single fuel cell using a GRandalytics test station. Standardized single fuel cell testing protocols were used for recording spatially resolved data. All experiments were carried out under galvanostatic control of the total cell current.

The segmented cell system consists of the cell hardware, the custom designed current transducer system, the data acquisition device and a single cell test station.[33] The system allows the data collection from 10 current channels in a high (standard) current mode and from 10 channels in a low current mode. The standard current mode enables

*Electrochemical Society Active Member.
[z]E-mail: A.Kulikovsky@fz-juelich.de

the measurement of segment current densities up to 2 A cm^{-2}. The low current mode yields measurement of current up to 50 mA cm^{-2}, which is typical for electrochemical diagnostics. Voltage and current signal data collection was performed with a National Instrument PXI data acquisition instrument operating on HNEI–developed LabView programs.

The segmented cell hardware consists of ten flow field segments forming a continuous path along ten parallel serpentine channels. Each segment is equipped with its own current collector and GDL and it has an area of 7.6 cm^2. The segmented hardware is applicable to either the anode or the cathode. The same channel designs are used for both the segmented and the standard flow fields (the reactant streams were arranged in a co-flow configuration).

The segmented cell was operated with commercially available 100 cm^2 membrane/electrode assembly (MEA) from Gore. The Pt/C loading of the anode and cathode electrodes was 0.4 mgPt cm^{-2}. Sigracet 25 BC was used as the anode and cathode gas diffusion layers (GDLs). The cathode used a segmented GDL and gasket configuration, whereas a uniform GDL was applied at the anode. The total active area of MEA was 76 cm^2. The gasket material was made of Teflon, with thicknesses of 125 μm for the anode and cathode.

The segmented cell was assembled, conditioned and tested by making the polarization curve measurements. The anode/cathode conditions were hydrogen/air at 2/2 and 2/10 stoichiometry, 100/50% relative humidity and ambient pressure. The cell temperature was 70°C. The frequency range for the EIS measurements was 0.05 Hz to 10 kHz and the amplitude of the sinusoidal current perturbation corresponded to the amplitude of the cell voltage response of 10 mV or lower. The impedance spectra were collected at the cell current density of 50 mA cm^{-2}.

Model

Model parameters and impedances.—The q2D model[8] has been developed for the linear segmented cell shown schematically in Figure 1. The total impedance Z_c of the cathode side (Figure 1) is a sum of parallel local impedances

$$\frac{1}{Z_c} = \sum_{n=1}^{N} \frac{1}{Z_{ccl,n} + Z_{gdl,n}} \quad [1]$$

where $Z_{ccl,n}$ is the local impedance of the cathode catalyst layer (CCL), $Z_{gdl,n}$ is the local impedance of the gas–diffusion layer (GDL), and N is the number of segments. In the limit of infinite number of segments, Eq. 1 transforms to

$$\frac{1}{Z_c} = \frac{1}{L}\int_0^L \frac{dz}{Z_{ccl}(z) + Z_{gdl}(z)} \quad [2]$$

where $Z_{ccl}(z)$ and $Z_{gdl}(z)$ are continuous functions of the coordinate z along the air channel, and L is the channel length. In the following, we will also use the total GDL impedance Z^{λ}_{gdl} defined as

$$\frac{1}{Z^{\lambda}_{gdl}} = \frac{1}{L}\int_0^L \frac{dz}{Z_{gdl}(z)} \quad [3]$$

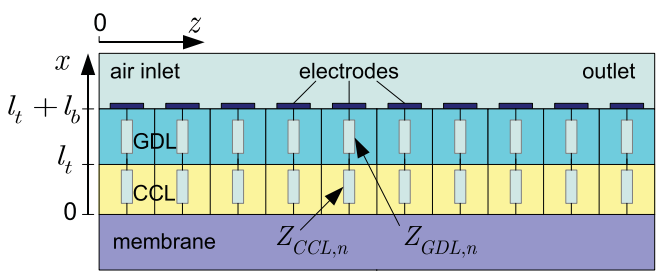

Figure 1. Schematic of the segmented cathode side of a fuel cell used in modeling.

and the shifted along the real axis GDL impedance $Z^{\lambda}_{gdl,s}$, calculated using the following relation

$$\frac{1}{Z^{\lambda}_{gdl,s}} = \frac{1}{L}\int_0^L \frac{dz}{R_{ccl} + Z_{gdl}} \quad [4]$$

where

$$R_{ccl} = \frac{l_t}{3\sigma_p} + \frac{b}{j_0} \quad [5]$$

is the static resistivity of the CCL with fast oxygen transport.[23] Here

$$j_0 = f_\lambda J\left(1 - \frac{1}{\lambda}\right)^{z/L} \quad [6]$$

is the local current density in the cell,[38] and

$$f_\lambda = -\lambda \ln\left(1 - \frac{1}{\lambda}\right) \quad [7]$$

is a function of the air flow stoichiometry λ defined as

$$\lambda = \frac{4Fhv^{in}c_h^{in}}{LJ}. \quad [8]$$

In the equations above, l_t is the CCL thickness, b is the ORR Tafel slope, σ_p is the CCL proton conductivity, j_0 is the local cell current density, h is the channel height, v^{in} is the inlet flow velocity, c_h^{in} is the inlet oxygen molar concentration, and J is the mean current density in the cell.

Analytical expressions for Z_{ccl} and Z_{gdl} were obtained in Ref. 23 and Ref. 7, respectively. Note that both the local Z_{gdl} and the total Z^{λ}_{gdl} GDL impedances include the impedance due to the air flow in the channel. Equations[7] show that Z_{gdl} and Z^{λ}_{gdl} depend on the oxygen concentration perturbation c_h^1 in the channel, while $Z_{ccl}(z)$ is independent of c_h^1, and hence it does not include the channel impedance. Therefore, the term "GDL impedance" is used below to denote the impedance of the system "GDL + flow field", i.e., the general equation for the GDL impedance includes the impedance due to the oxygen transport in the channel.

In the context of this work, of special interest is the total GDL impedance at infinite air stoichiometry $\tilde{Z}^{\infty}_{gdl}$:[8]

$$\tilde{Z}^{\infty}_{gdl} = \frac{\tan\left(\mu\tilde{l}_b\sqrt{-i\Omega/\tilde{D}_b}\right)}{\mu\sqrt{-i\Omega/\tilde{D}_b}(\tilde{D}_b - \tilde{J}\tilde{l}_b)(1 + i\Omega/\tilde{J})}, \quad \lambda \to \infty \quad [9]$$

where tilde marks the dimensionless variables

$$\tilde{l}_b = \frac{l_b}{l_t}, \quad \tilde{J} = \frac{Jl_t}{\sigma_p b}, \quad \tilde{Z} = \frac{Z\sigma_p}{l_t}, \quad \tilde{D}_b = \frac{4FD_b c_h^{in}}{\sigma_p b}. \quad [10]$$

The reduced dimensionless frequency Ω is given by

$$\Omega = \frac{\tilde{\omega}}{\varepsilon^2} \quad [11]$$

where

$$\tilde{\omega} = \omega t_*$$
$$t_* = \frac{C_{dl}b}{2i_*}. \quad [12]$$

Note that t_* is the characteristic time of double layer charging. The parameters ε and μ are

$$\varepsilon = \sqrt{\frac{\sigma_p b}{2i_* l_t^2}} \quad [13]$$

$$\mu = \sqrt{\frac{4Fc_h^{in}}{C_{dl}b}}. \quad [14]$$

Here l_b is the GDL thickness, ω is the circular frequency of the exciting signal ($\omega = 2\pi f$), C_{dl} is the double layer volumetric capacitance (F cm^{-3}), i_* is the ORR volumetric exchange current density (A cm^{-3}),

Table I. PEM fuel cell physical and operational parameters.

GDL thickness l_b, cm	0.022
CCL thickness, l_t, cm	0.0015
Channel height h, cm	0.1
Cell temperature T, K	273 + 70
Mean current density J, A cm^{-2}	0.05
Oxygen stoichiometry λ	2.0
Exchange current density i_*, A cm^{-3}	0.001

and D_b is the oxygen diffusion coefficient in the GDL. The superscript in marks the values at the channel inlet, and the subscripts h, b and t mark the values in the channel, GDL and CCL respectively.

The q2D model[8] and, in particular, Eq. 9 have been obtained assuming fast oxygen transport in the CCL. This limits the cell current densities, for which the model is applicable (see Discussion section). 1D model,[7] which is taken below for comparison with the q2D model, has been designed assuming that the contribution of impedances due to oxygen transport in the CCL and GDL to the total cell impedance is small, but non–negligible. Accurate least–squares fitting algorithm based on 1D model is able to capture these small contributions and it gives the respective transport parameters (see Ref. 7 for further discussion). Note also that at high λ, all the local GDL impedances in Figure 1 are the same, and hence Eq. 9 describes both the local and the total GDL impedances. It is also worth noting that Eq. 9 differs from the Warburg impedance for the transport layer of a finite thickness, due to the presence of the frequency–dependent factor $(1 + i\Omega/\tilde{J})$ in the denominator (see Ref. 8 for detailed discussion).

At what frequencies is the GDL impedance important?—To answer this question, we have to calculate the modulus $|\tilde{Z}^{\infty}_{gdl}|$. Direct calculation of $|\tilde{Z}^{\infty}_{gdl}|$ from Eq. 9 leads to a rational expression containing the terms with sin– and cos–functions, and with hyperbolic sinh– and cosh–functions of the same argument, given by the left side of Eq. 15. If this argument exceeds 2

$$\mu\tilde{l}_b\sqrt{\frac{2\Omega}{\tilde{D}_b}} > 2 \qquad [15]$$

the terms with the sin– and cos–functions can be neglected, and we come to

$$|\tilde{Z}^{\infty}_{gdl}| \simeq \frac{1}{\mu(\tilde{D}_b - \tilde{J}\tilde{l}_b)}\sqrt{\frac{\tilde{J}^2\tilde{D}_b}{\Omega(\Omega^2 + \tilde{J}^2)}} \qquad [16]$$

In dimensional form, Eq. 15 gives the minimal frequency $f_{\min}$, at which Eq. 16 holds:

$$l_b\sqrt{\frac{4\pi f}{D_b}} > 2, \quad \text{or} \quad f > f_{\min} = \frac{D_b}{\pi l_b^2} \qquad [17]$$

For the set of parameters in Tables I, II, Eq. 17 gives $f_{\min} \simeq 6.58$ Hz.

It is advisable to estimate $|\tilde{Z}^{\infty}_{gdl}|$ at the frequencies satisfying to Eq. 17. At small current densities $\tilde{J} \ll 1$, the CCL charge–transfer resistivity $1/\tilde{J}$ is much greater than unity. Thus, the condition $|\tilde{Z}^{\infty}_{gdl}| = 1$ gives the minimal frequency Ω_*, at which the contribution of $\tilde{Z}^{\infty}_{gdl}$ to the total impedance becomes small. Equating 16 to unity and solving the resulting cubic equation for Ω, we get a single real root of this equation:

$$\Omega_* = \frac{1}{6}\left(\left[\frac{12\tilde{J}^2\left(\sqrt{12A^4\tilde{J}^2 + 81\tilde{D}_b^2} + 9\tilde{D}_b\right)}{A^2}\right]^{1/3} - \left[\frac{(12A\tilde{J}^2)^2}{\sqrt{12A^4\tilde{J}^2 + 81\tilde{D}_b^2} + 9\tilde{D}_b}\right]^{1/3}\right) \qquad [18]$$

where

$$A = \mu(\tilde{D}_b - \tilde{J}\tilde{l}_b) \qquad [19]$$

From Eq. 16 it follows that $|\tilde{Z}^{\infty}_{gdl}|$ decays with Ω as $\Omega^{-3/2}$; thus, for $\Omega > \Omega_*$, the contribution of the GDL impedance to the total cell impedance is small and it progressively decreases with Ω. The dimensional regular frequency f_* corresponding to Ω_* is

$$f_* = \frac{\varepsilon^2\Omega_*}{2\pi t_*} = \frac{\sigma_p\Omega_*}{2\pi l_t^2 C_{dl}} \qquad [20]$$

where t_* given by Eq. 12 was used.

With the data from Tables I, II, Eq. 20 gives

$$f_* \simeq 3.74\,\text{Hz}$$

Noting that Eq. 17 must also be fulfilled, we finally get the following condition for the regular frequencies, at which $|\tilde{Z}^{\infty}_{gdl}|$ is small:

$$f > f_{\lim} = \max\left\{f_{\min} = \frac{D_b}{\pi l_b^2},\, f_* = \frac{\sigma_p\Omega_*}{2\pi l_t^2 C_{dl}}\right\} \qquad [21]$$

With the data in Tables I, II, Eq. 21 holds for the frequencies $f >$ 10 Hz.

Note that the condition Eq. 17 is sufficient, but not necessary. This condition determines validity of Eq. 16, which simplifies the analysis above. If, however, the GDL diffusivity $\tilde{D}_b$ is large, Eq. 17 could be restrictive. For $\tilde{D}_b \to \infty$, from Eq. 9 we find

$$|\tilde{Z}^{\infty}_{gdl}| \simeq \frac{\tilde{l}_b}{\tilde{D}_b\sqrt{1 + (\Omega/\tilde{J})^2}}, \quad \tilde{D}_b \to \infty$$

From this equation it follows, that at large $\tilde{D}_b$, $|\tilde{Z}^{\infty}_{gdl}| < 1$ at all frequencies Ω, or, equivalently, at all regular frequencies f.

Clearly, at any *finite* stoichiometry λ, the total GDL impedance $\tilde{Z}^{\lambda}_{gdl}$ satisfies to

$$|\tilde{Z}^{\lambda}_{gdl}| > |\tilde{Z}^{\infty}_{gdl}| \qquad [22]$$

At low frequencies, the inequality 22 holds with a large margin, as finite λ dramatically increases $|\tilde{Z}^{\lambda}_{gdl}|$ due to a finite rate of oxygen transport in the channel (Figure 2a). However, with the growth of the frequency Ω, $|\tilde{Z}^{\lambda}_{gdl}|$ tends to $|\tilde{Z}^{\infty}_{gdl}|$.

This effect is illustrated in Figure 2, which shows the model spectra of the total dimensionless cell impedance $\tilde{Z}_c$, Eq. 2, at various stoichiometries of the air flow. Figures 2b, 2c show the spectra of the shifted total GDL impedance $\tilde{Z}^{\lambda}_{gdl,s}$, Eq. 4, for the several values of λ. As can be seen, starting from a certain frequency, the finite–λ GDL impedance $\tilde{Z}^{\lambda}_{gdl,s}$ approaches the infinite–λ impedance $\tilde{Z}^{\infty}_{gdl,s}$, represented by the curve for λ = 100 in Figure 2c. The higher the stoichiometry λ, the closer to $\tilde{Z}^{\infty}_{gdl,s}$ is located the respective curve $\tilde{Z}^{\lambda}_{gdl,s}$ (Figure 2c). Thus, at a certain frequency, the inequality in Eq. 22 transforms into "approximately equals to" sign. From this frequency on, both the sides of Eq. 22 are close to each other and small, and according to Eq. 16, they decay as a power function of Ω, $|\tilde{Z}^{\lambda}_{gdl}| \simeq |\tilde{Z}^{\infty}_{gdl}| \sim \Omega^{-3/2}$ (Figure 2c).

The data plotted in Figure 2 show that the frequency separating the regions of exponential and power decay of $\tilde{Z}^{\lambda}_{gdl}$ with Ω is f_*,

Table II. The average cell parameters resulted from impedance spectra fitting. The cell current density is 50 mA cm^{-2}.

	λ = 2	λ = 10
Tafel slope b, V	0.031	0.032
CCL proton conductivity σ_p, Ω^{-1} cm^{-1}	0.02	0.01
Double layer capacitance C_{dl}, F cm^{-3}	22	20
Oxygen diffusion coefficient in the CCL D, cm^2 s^{-1}	$0.6 \cdot 10^{-4}$	$0.5 \cdot 10^{-4}$
Oxygen diffusion coefficient in the GDL D_b, cm^2 s^{-1}	0.01 (variable)	0.008 (variable)
Average effective air stoichiometry	6.28	–

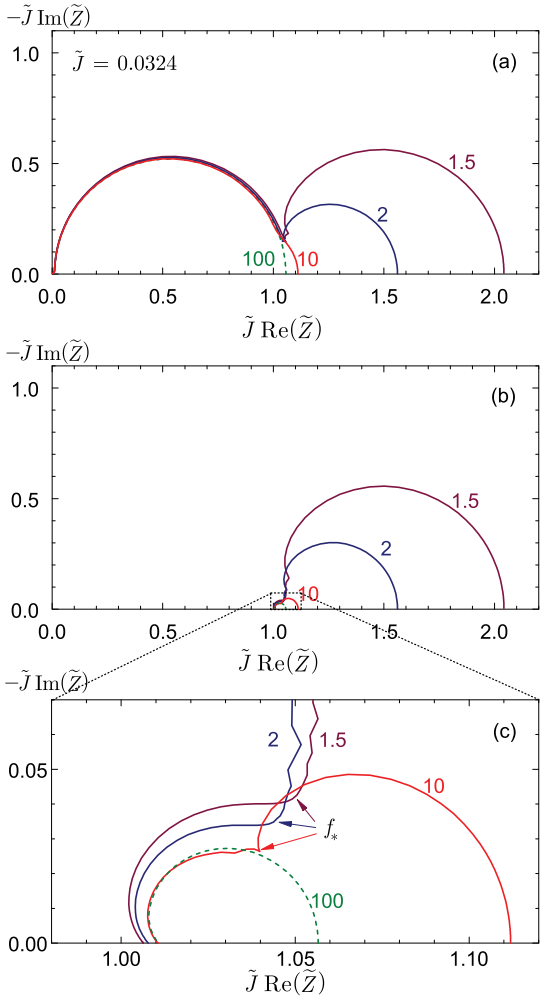

Figure 2. (a) q2D model spectra for the indicated values of the flow stoichiometry λ. Note the coordinates $\tilde{J}\tilde{Z}$. (b) Contributions due to the oxygen transport in the GDL and channel to the total impedance spectra. Note a very fast decay of this contribution with the frequency growth. (c) Zoomed window in (b). Parameters for calculations are listed in Tables I, II.

Eq. 20 (arrows in Figure 2c). Unfortunately, we were not able to perform a formal proof of this statement due to unmanageable complex expressions; however, numerical tests confirm this result. It follows, that for the frequencies satisfying to Eq. 21, we may use the respective part of the impedance spectrum for fitting the 1D model[7] to *this part of the spectrum only*. Clearly, the same is true for the local GDL impedances, as integration along z in Eq. 3 does not affect the frequency dependence of the functions on the left and right side. The 1D model[7] includes the GDL impedance at infinite stoichiometry λ, and hence we may expect determination of $\tilde{D}_b$ from such fitting.[d]

Fitting Results and Discussion

Low air flow stoichiometry (λ = 2).—Before fitting, the raw impedance spectra have been processed according to the following protocol. The high–frequency points with the positive imaginary part have been excluded from consideration, as these points exhibit the effect of cable inductance. Further, the remaining high–frequency points (in the frequency range between 1 kHz and 123 Hz) have also been excluded from fitting. These points exhibit the arc of yet undefined nature.[39,40] Similar arc has been detected in our experiments with the pure oxygen feed.[29] Here this arc is less pronounced; nonetheless, it "hides" the high–frequency straight line with the 45°–slope, which describes proton transport in the CCL.[23,41]

Generally, there are two options to treat this arc. The first one is to model the arc by a parallel *RC*–circuit; this approach has been taken in Ref. 29. It gives good quality of spectra fitting in the high–frequency (HF) domain; however, the resulting CCL proton conductivity σ_p seems to be overestimated by a factor of two to three.[29] In this work, we simply ignored the HF arc points by setting in the fitting algorithms the respective weight factors to zero. This approach results in minimal variation of σ_p between different segments, as discussed below; moreover, the values of σ_p agree well with the literature data. Is is important to emphasize that both the approaches affect only the value of σ_p, leaving the other parameters practically intact.

Least–squares fitting has been performed in Maple environment using the matrix form of *NonlinearFit* procedure. Fitting of a single impedance spectrum using 1D and q2D models takes less than one minute on a standard PC. The Maple worksheet with the 1D model fitting code is available for download at *https://github.com/akulikovsky/Fitting_Procs/issues/1*. Figure 3 shows the experimental spectra (points) of individual segments fitted using the two models: the dashed lines represent the q2D model[8] fitted to the full set of the experimental points, while the solid lines show the 1D model[7] fitted to the points satisfying to Eq. 21. While fitting the 1D model, the measured local current density in the segments was used and the local oxygen concentration in the channel was calculated according to [38]

$$c_h(z) = c_h^{in}\left(1 - \frac{1}{\lambda}\right)^{z/L} \qquad [23]$$

Measured local current density in each segment is shown in Figure 4. For comparison, the "ideal" 1D distribution of local current (Eq. 6) corresponding to the straight–channel cell[38] is also shown in this Figure. The experimental and fitted spectra of the whole fuel cell for the current density of 50 mA cm^{-2} and the stoichiometry of λ = 2 are shown in Figure 5.

The q2D model was fitted to the data assuming that the flow stoichiometry λ is a fitting parameter. We were not able to obtain good quality of fitting with the fixed stoichiometry of λ = 2. The reason is that the q2D model is constructed for a linear cell with a straight air channel, while in experiment we employed a true 2D cell with meander–like channels.[33] In a cell with the meander–like flow field, oxygen is transported between the adjacent turns of the meander due to under–rib diffusion and convection; these processes are ignored in the q2D model. Indeed, Figure 4 shows that in segments 6–9, the local current exceeds the 1D value. We attribute this effect to under–rib oxygen transport in the cell, which homogenizes oxygen distribution over the cell surface. Treating λ as a fitting parameter allows us to obtain the effective stoichiometry λ_{eff}, which in effective manner describes the quality of the oxygen distribution over the cell surface. For the air stoichiometry of λ = 2, the average value of λ_{eff} is 6.28 (Table II). This issue will be discussed in more detail in a separate publication.

Based on the quality of fitting, two domains can be distinguished in the cell. The first domain resides close to the oxygen channel inlet (segments 1 to 4). In this domain, both the 1D and q2D models fit the data reasonably well (Figure 3). In the second domain located in the middle and "remote" parts of the cell (segments 5–10) the quality of data fitting by the q2D model[8] progressively worsens toward the outlet. In 10-th segment, no successful fitting was obtained with this model (Figure 3). In contrast, in all the segments, the solid curves representing the 1D model[7] fit well the "faradaic" arc (Figure 3).

Comparison of the fitting parameters obtained with the two models is shown in Figure 6; the open circles represent the q2D model, while the filled circles correspond to the 1D model. Dotted lines show the average over the the cell surface parameters from the 1D model (Figure 6). The results from the two models are close to each other; however, due to higher quality of data fitting, the 1D model results seem to be more reliable, as they exhibit smaller variation over the cell surface. The Tafel slopes resulted from the two models are close

[d]Figure 2c suggests that f_* separates the channel impedance ($f < f_*$) and the pure GDL impedance ($f > f_*$) corresponding to non-uniform oxygen concentration along the channel. (Note added while proofreading.)

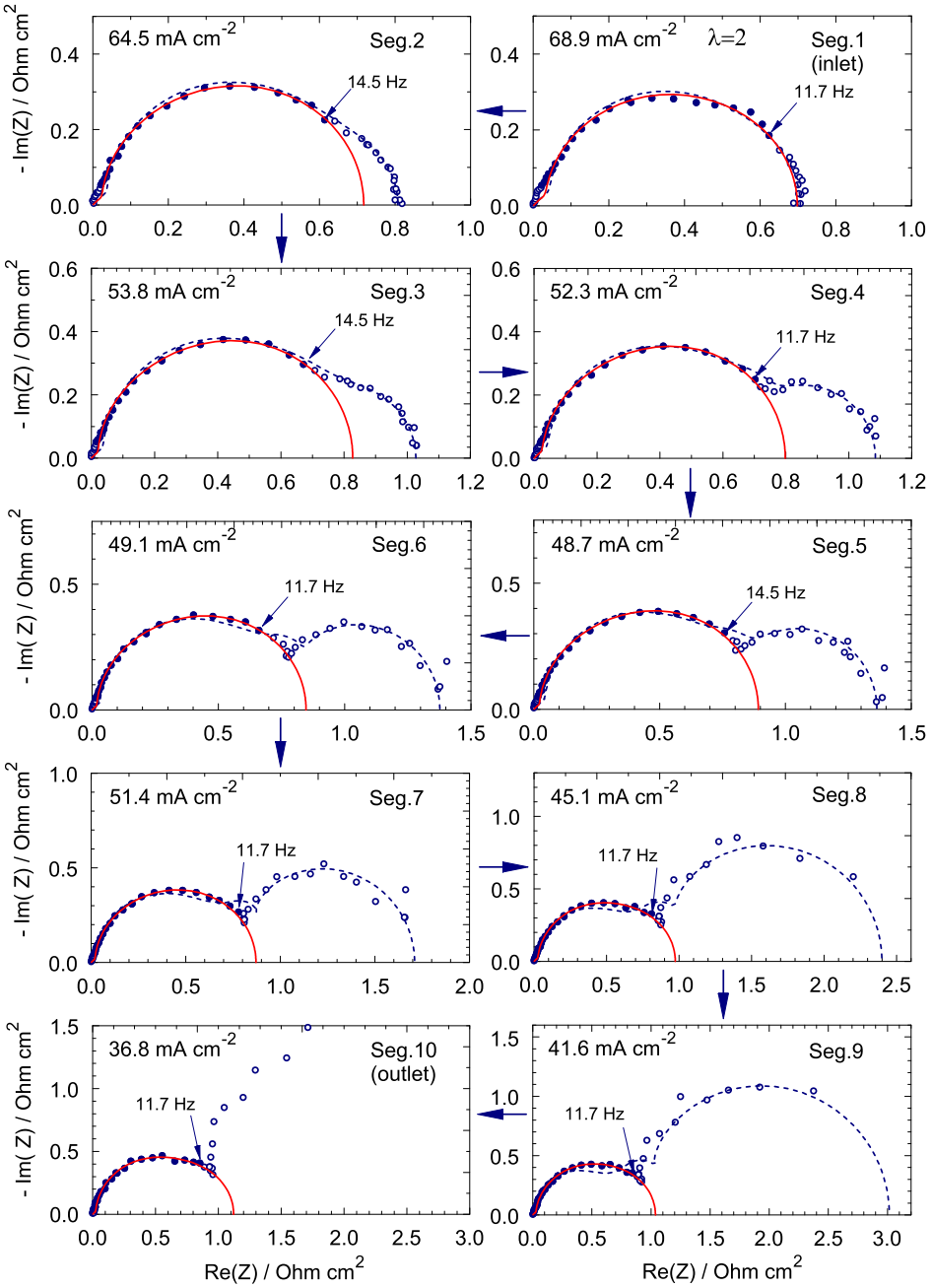

Figure 3. The experimental (points) and fitted (lines) spectra for the oxygen stoichiometry of $\lambda = 2$. Oxygen inlet is at segment 1; the bold arrows indicate the direction of the air flow. Dashed lines show the q2D model fitted to the complete set of experimental points. The solid lines exhibit the 1D model fitted to the sufficiently high–frequency points, with f satisfying to Eq. 21. The data for the last segment 10 has not been fitted by the q2D model due to large noise in the low–frequency points. Inside each frame, small arrows indicate the most low–frequency point used for the 1D model fitting.

to each other (Figure 6a). The variation of b along the channel from the 1D model is minimal and it follows the shape of the local current density (cf. filled circles in Figure 6a and in Figure 4).

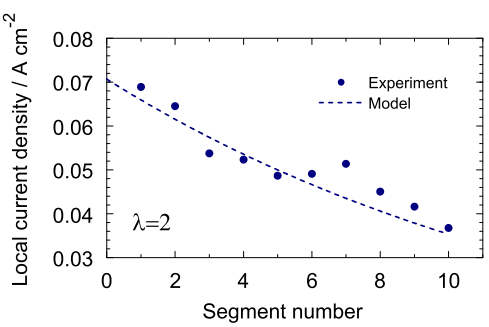

Figure 4. Measured (points) and model, Eq. 6, local current densities in the cell.

The 1D model gives fairly uniform CCL proton conductivity over the cell surface (Figure 6b), with the surface–average value of 0.02 Ω^{-1} cm^{-1}. This value is close to σ_p reported in Ref. 41 (0.01 to 0.03 Ω^{-1} cm^{-1}) from impedance measurements. The q2D model gives somewhat lower surface–average σ_p, though it is close to 0.02 Ω^{-1} cm^{-1} (Figure 6b). The double layer capacitances from the 1D and the q2D models are also close to each other; the surface–average value of 22 F cm^{-3} agrees well with the literature data[41] (Figure 6c). The 1D model gives the oxygen diffusion coefficient D_{ox} in the CCL, a parameter, which cannot be obtained from the q2D model (Figure 6d). The average over the cell surface value of D_{ox} is about $6 \cdot 10^{-5}$ cm^2 s^{-1}, which agrees with the oxygen diffusivity in water at 70°C.[42] Molecular dynamics simulations of Malek, Mashio and Eikerling[43] show that the thickness of Nafion film covering Pt/C agglomerates in the CCL does not exceed ten nanometers. Elementary estimate shows that oxygen penetrates through such a thin film without sizeable losses. Thus, most of the oxygen transport losses in the CCL occur in the void space between Pt/C agglomerates. The value of D_{ox}

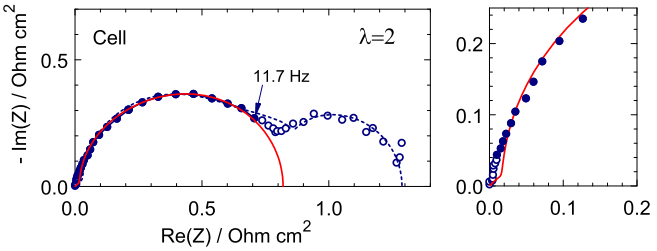

Figure 5. The impedance spectrum of the whole fuel cell for $\lambda = 2$. Points – the experimental data, dashed lines – the q2D model fitted to all the data, solid lines – 1D model fitted to the filled circles only. The fitting parameters are indicated in Figure 6 as zero segment points. The right panel shows the high–frequency part of the spectrum.

above suggests that this space is severely flooded (see also Discussion section).

The shape of the oxygen diffusivity D_b in the GDL along the oxygen channel, which results from the 1D model is shown in Figure 6d. The surface–average value of this parameter is about 0.01 cm^2 s^{-1}; however, D_b exhibits distinct decay toward the channel outlet, which suggests progressive GDL flooding along z (Figure 6d). The surface–average $D_b \simeq 0.01$ cm^2 s^{-1} seems to be reasonable, as the GDL in our cell is equipped with the micro–porous layer (MPL), which lowers the effective diffusivity of the system "GDL+MPL". In our experiments, the MPL thickness is $\sim$50 μm, and the MPL has similar to the CCL values of porosity and pore size.[44–49] Note that no data on in situ measurements of D_b are available in literature.

The "GDL" oxygen diffusivity resulted from the q2D model is indicated in Figure 6e together with the average diffusion coefficient D_{eff} *in the CCL and the GDL*, resulted from the 1D model. The latter parameter has been calculated according to

$$\frac{l_t + l_b}{D_{eff}} = \frac{l_t}{D_{ox}} + \frac{l_b}{D_b} \qquad [24]$$

As can be seen, calculated D_{eff} is close to the value of the "GDL diffusivity", resulted from the q2D model (Figure 6e). This suggests, that the q2D model gives, in fact, the average (effective) oxygen diffusion coefficient in the CCL and the GDL. The oxygen transport in the CCL is ignored in the q2D model, and this model assigns the respective transport loss to the GDL. Similar effect has been observed in Refs. 28 and 7. In Ref. 28, the impedance model of the CCL only was fitted to the experimental spectrum; in Ref. 7, the "CCL+GDL" model was fitted to *the same spectrum*. In both the cases, oxygen transport in the CCL was taken into account. The results show that the GDL transport loss, which is ignored in the CCL–only model, simply reduces the effective CCL oxygen diffusivity, not changing the other model parameters. We can cautiously conclude, that the neglect of either CCL, or GDL oxygen diffusion in the impedance models discussed changes only the diffusion coefficient of the layer, which has been taken into account. In other words, by ignoring the oxygen transport in the CCL in the q2D model, we only get lower value of the oxygen diffusion coefficient in the GDL from this model, not changing the other physical parameters.

The parameters resulted from fitting the spectra of the whole fuel cell (Figure 5) are shown in Figure 6 as the zero–segment data. These parameters are not far from the surface–average data, indicated by the dashed lines in Figure 6. Thus, the results of this work are valid for the spectra measured with standard non–segmented cells.

***High air flow stoichiometry* ($\lambda = 10$).—**The idea of using the 1D model for fitting the HF part of the low-lambda spectra can be verified by measuring the local spectra for the same MEA under high stoichiometry of the flow, when the λ–effects vanish. Comparison of the 1D fitting parameters for these spectra to the parameters obtained in the previous subsection could justify this approach.

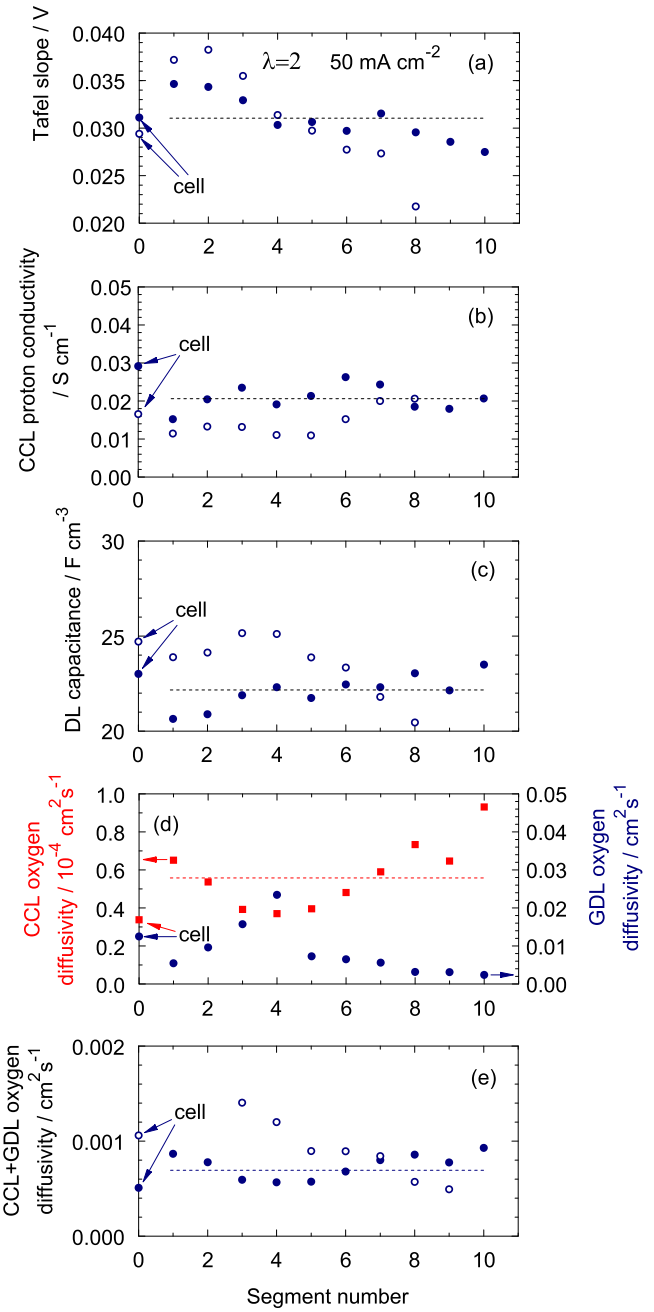

Figure 6. The fitting parameters for the segments 1–10 for the flow stoichiometry of $\lambda = 2$ and the cell current density of 50 mA cm^{-2}. Open circles show the parameters obtained from the q2D model [8] (see dashed curves in Figure 3), while the filled circles display the results from the 1D model[7] (solid curves in Figure 3). Filled circles in Figure 6 e are calculated using Eq. 24. Dotted lines indicate the average parameters from the 1D model. The parameters obtained from fitting the spectra of the whole cell (see Figure 5) are indicated as the "zero segment" data.

The experimental and fitted 1D model local spectra for $\lambda = 10$ are shown in Figure 7. Note a quite well expressed second (low–frequency) arc in the last segments (7 to 10). This arc arises due to progressive worsening of the oxygen transport in the GDL in the direction of air flow. Even at the current density of 50 mA cm^{-2}, liquid water tends to accumulate in the last segments of the cell, and it reduces the GDL oxygen diffusivity in these segments. This effect is clearly seen in Figure 8, which shows the fitting parameters for the curves in Figure 7. The GDL diffusion coefficient D_b decreases

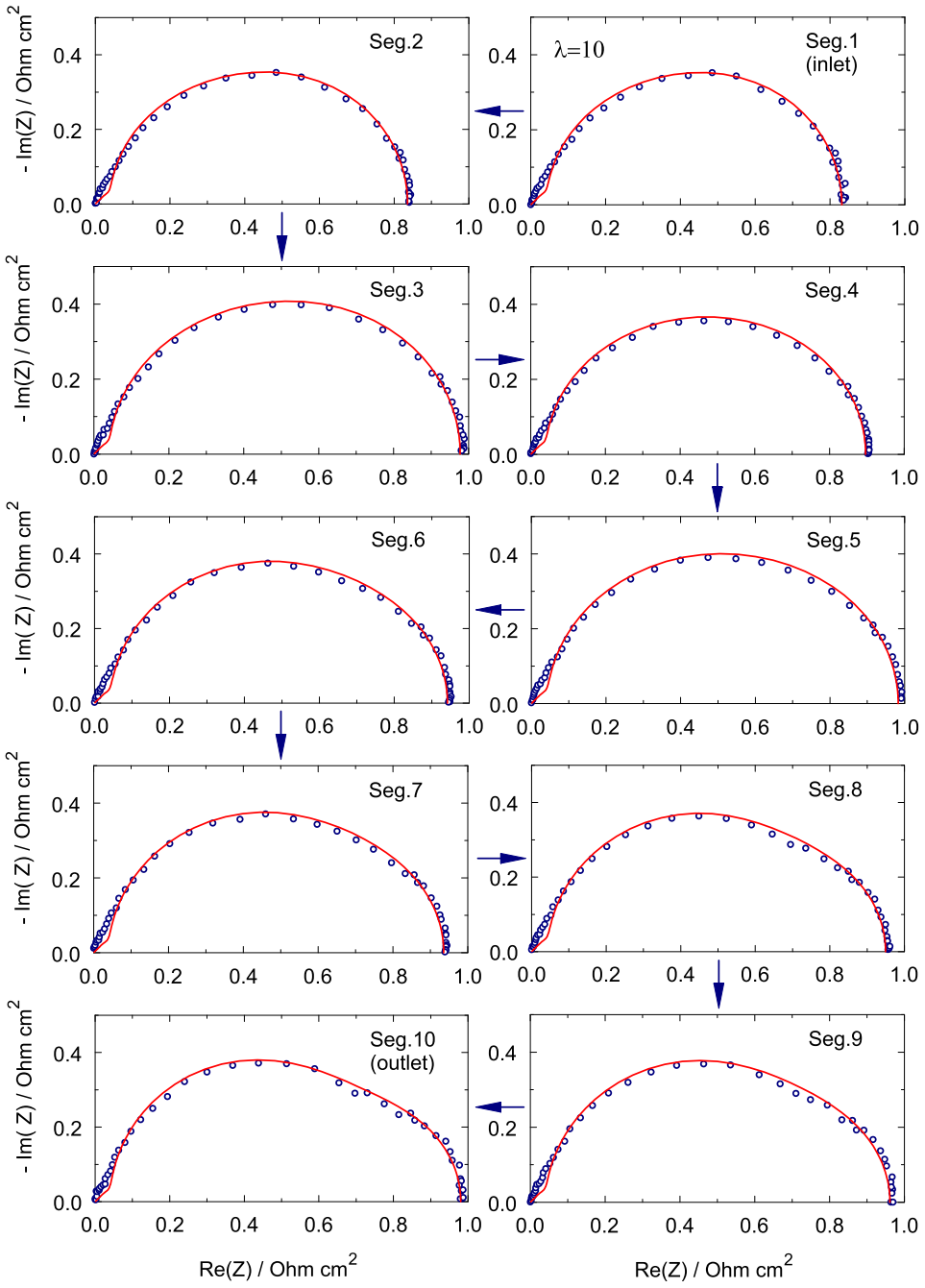

Figure 7. The experimental (points) and fitted 1D model (lines) spectra for the flow stoichiometry of $\lambda = 10$. Oxygen inlet is at segment 1; arrows indicate the direction of the air flow.

toward the channel outlet (Figure 8d). The same trend exhibits D_b in Figure 6d.

The other parameters in Figure 8 agree with those obtained in the regime with $\lambda = 2$ (Figure 6). The only exception is the CCL proton conductivity, which appears to be twice lower in the regime with $\lambda = 10$ (cf. Figures 6b and 8b). Note that the spread of the points in Figure 8b is minimal, i.e., σ_p is fairly uniform along the cell surface. Lower conductivity in the regime with $\lambda = 10$ can be explained by a faster rate of liquid water removal from the cell by the air flow of a higher velocity.

Twice lower σ_p in the regime with $\lambda = 10$ qualitatively agrees with the growth of the high–frequency resistivity (HFR) of the cell, defined as the shift of the raw impedance spectra from the origin of coordinate along the real axis. The dominating part of this resistivity is due to the proton transport in membrane. Table III shows that the higher air flow velocity lowers the membrane proton conductivity, seemingly due to faster liquid water removal from the cell.

Discussion.—Both the 1D and the q2D models are valid provided that the cell current density J is low:[7,8]

$$J \ll \min\left\{ j_* = \frac{\sigma_p b}{l_t},\ j_D = \frac{4FD_{ox}c_1}{l_t} \right\} \qquad [25]$$

Here, j_* and j_D are the characteristic current densities for proton and oxygen transport in the CCL, respectively, and c_1 is the oxygen concentration at the CCL/GDL interface. For the estimate, at the cell current density of 50 mA cm^{-2} we can neglect the oxygen transport losses in the GDL and set c_1 equal to the oxygen concentration in air. With the parameters in Table I and in Figure 6, we get $j_* \simeq 450$ mA cm^{-2} and $j_D \simeq 100$ mA cm^{-2}. Thus, the inequalities $J \ll j_*$ and $J < j_D$ hold rather than Eq. 25, which means that the experimental spectra could be slightly depressed due to the oxygen transport in the CCL. This depression has been ignored in the analysis above.

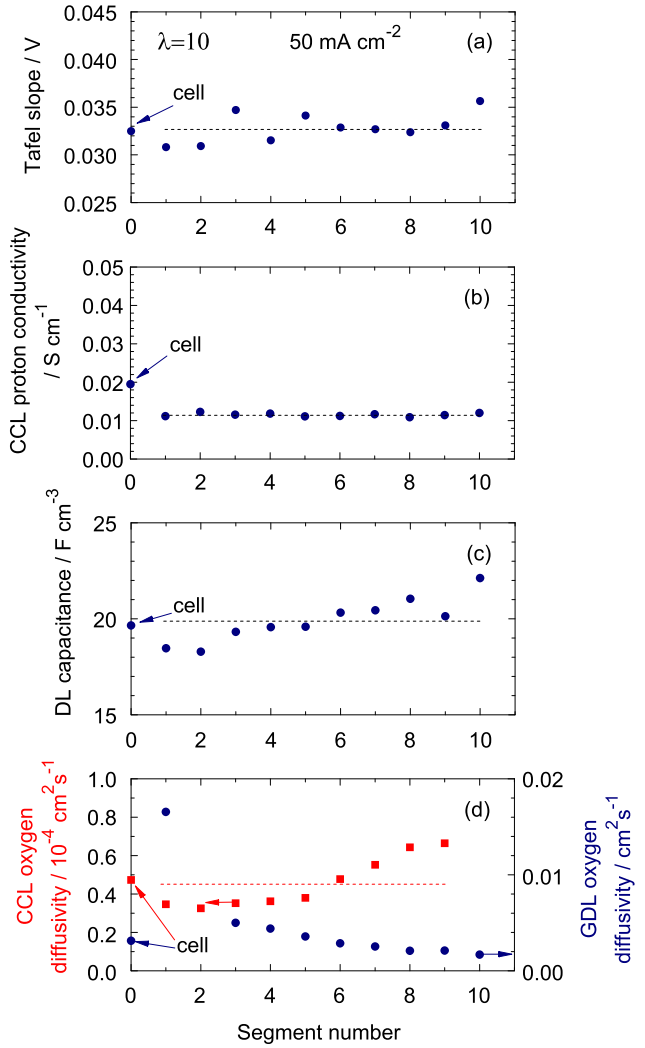

Figure 8. The fitting parameters for the segments 1–10 for the flow stoichiometry of $\lambda = 10$ and the cell current density of 50 mA cm^{-2}. The filled circles display the results from the 1D model fitted to the data.[7] Dotted lines indicate the average over the cell surface parameters. The parameters obtained from fitting the spectra of the whole fuel cell are indicated as the "zero segment" data.

The parameter j_D indicates the cell current density, above which the Tafel slope doubling due to oxygen transport in the CCL occurs. However, this parameter itself changes with the cell current density due to shift in the balance of water production, evaporation, condensation and transport rates in the CCL. Low value of j_D obtained above can be corrected based on the following arguments.

Low value of the oxygen diffusion coefficient in the CCL $D_{ox} \simeq 6 \cdot 10^{-5}$ cm^2 s^{-1} (Figure 6) suggests that significant fraction of oxygen is transported through the CCL in dissolved form. At the temperature of 70°C, the dimensionless Henry constant H_{ox} for oxygen in water is about 0.11. Thus, if all the oxygen were transported in the dissolved form, the effective CCL oxygen diffusivity would be $D_{ox}/H_{ox} \simeq 5 \cdot 10^{-4}$ cm^2 s^{-1}, which is ten times larger, than the oxygen diffusivity in water. This estimate suggests that there are parallel "channels" for gaseous and dissolved oxygen transport in the CCL, and that oxygen fluxes in these channels are of the same order of magnitude. A more accurate account of oxygen transport in the CCL requires incorporation of gaseous and dissolved transport mechanisms into the model. This would increase the effective average oxygen diffusion coefficient in the CCL up to the value between $5 \cdot 10^{-4}$ and $6 \cdot 10^{-5}$ cm^2 s^{-1}, and hence it would lead to larger value of j_D.

Table III. The local high–frequency resistivity of the cell (Ω cm^2) in the regimes with the air flow stoichiometry 2 and 10.

Segment	HFR@$\lambda = 2$	HFR@$\lambda = 10$
01	0.0607	0.0719
02	0.0626	0.0755
03	0.0637	0.0772
04	0.0493	0.0655
05	0.0557	0.0704
06	0.0538	0.0684
07	0.0553	0.0697
08	0.0510	0.0642
09	0.0514	0.0613
10	0.0527	0.0610

Conclusions

We measure local impedance spectra of the segmented cell operated at the air flow stoichiometry of $\lambda = 2$. The spectra have been fitted using the two recent physical models for the PEMFC impedance. The 1D model assumes infinite rate of the oxygen transport in the channel, while the quasi–2D model takes into account a finite rate of this transport. Analysis of the q2D equation for the total GDL impedance at an infinite stoichiometry of the air flow shows that this impedance rapidly decays with the growth of the frequency of the exciting signal. We derive an equation for the boundary frequency $f_{\rm lim}$ and show that starting from $f \simeq f_{\rm lim}$, the contribution of the oxygen transport in the system "channel + GDL" to the total cell impedance is small. This allows us to fit the 1D model to the points with $f > f_{\rm lim}$ only. Therefore, the q2D model has been fitted to the full set of impedance points, while the 1D model has been fitted to the points with $f > f_{\rm lim}$ only. The quality of curve fitting with the 1D model appears to be high. The fitting parameters resulted from the 1D and q2D models agree well, though the q2D model gives larger spread of parameters between the individual segments.

In addition, the local spectra for $\lambda = 10$ have been measured and fitted using the 1D model. The resulting set of fitting parameters agrees well with the set obtained in the case of $\lambda = 2$, except the CCL proton conductivity, which appears to be twice lower. We attribute this to a faster rate of liquid water removal from the cell by the air flow of a higher velocity. We conclude that the 1D model can be used for characterization of a PEM fuel cell running at a low stoichiometry of the air flow, provided that the impedance points satisfying to Eq. 21 are taken for fitting.

Acknowledgments

T. Reshetenko is grateful to funding from US Office of Naval Research (N00014-11-1-0391), US Army Research Office (W911NF-15-1-0188) and the Hawaiian Electric Company for ongoing support of the Hawaii Sustainable Energy Research Facility.

List of Symbols

~	Marks dimensionless variables
b	Tafel slope, V
C_{dl}	Double layer volumetric capacitance, F cm^{-3}
c	Oxygen molar concentration in the CCL, mol cm^{-3}
c_h	Oxygen molar concentration in the channel, mol cm^{-3}
c_h^{in}	Oxygen molar concentration at the channel inlet, mol cm^{-3}
D_{ox}	Oxygen diffusion coefficient in the CCL, cm^2 s^{-1}
D_b	Oxygen diffusion coefficient in the GDL, cm^2 s^{-1}
F	Faraday constant, C mol^{-1}
f	Regular frequency, Hz
f_λ	Function of the oxygen stoichiuometry λ, Eq. 7
J	Mean current density in the cell, A cm^{-2}
j_0	Local cell current density, A cm^{-2}

j_*	Characteristic current density for proton transport in the CCL, Eq. 25, A cm^{-2}
j_D	Characteristic current density for oxygen transport in the CCL, Eq. 25, A cm^{-2}
h	Channel height, cm
i	Imaginary unit
i_*	Volumetric exchange current density, A cm^{-3}
L	Channel length, cm
l_b	Gas–diffusion layer thickness, cm
l_t	Catalyst layer thickness, cm
N	Number of segments of the segmented cathode
R_{ccl}	Static differential resistivity of the CCL, Ω cm^2
t	Time, s
t_*	Characteristic time, s, Eq. 12
v	Air flow velocity in the channel, cm s^{-1}
x	Coordinate through the cell, cm
z	Coordinate along the channel, cm
Z_c	Total impedance of the cathode side, Ω cm^2
Z_{ccl}	Local CCL impedance, Ω cm^2
Z_{gdl}	Local GDL impedance, Ω cm^2
Z^{λ}_{gdl}	Total GDL impedance, Eq. 3, Ω cm^2
$Z^{\lambda}_{gdl,s}$	Total shifted GDL impedance, Eq. 4, Ω cm^2

Greek

ε	Newman's dimensionless reaction penetration depth, Eq. 13
η	ORR overpotential (positive by convention), V
λ	Stoichiometry of the oxygen flow, Eq. 8
μ	Dimensionless parameter, Eq. 14
σ_p	CCL ionic conductivity, Ω^{-1} cm^{-1}
Ω	Dimensionless reduced circular frequency, Eq. 11
ω	Circular frequency ($\omega = 2\pi f$), s^{-1}

Subscripts

0	Membrane/CCL interface
1	CCL/GDL interface
b	GDL
c	cathode
t	Catalyst layer
$*$	Characteristic value

Superscripts

1	Small–amplitude perturbation
∞	Infinite oxygen stoichiometry
in	Oxygen channel inlet

References

1. M. E. Orazem and B. Tribollet, *Electrochemical Impedance Spectroscopy*, Wiley, New–York, 2008.
2. A. Lasia, *Electrochemical Impedance Spectroscopy and its Applications*, Springer, New York, 2014.
3. E. Warburg, *Ann. Physik und Chemie*, **67**, 493 (1899).
4. H. Gerischer, *Z. Physik. Chem.*, **198**, 286 (1951).
5. S. Arisetty et al., *J. Electrochem. Soc.*, **159**, B455 (2012).
6. M. S. Kondratenko, M. O. Gallyamov, and A. R. Khokhlov, *Int. J. Hydrogen Energy*, **37**, 2596 (2012).
7. A. A. Kulikovsky, *J. Electrochem. Soc.*, **162**, F217 (2015).
8. A. Kulikovsky and O. Shamardina, *J. Electrochem. Soc.*, **162**, F1068 (2015).
9. T. E. Springer, T. A. Zawodzinski, M. S. Wilson, and S. Gottesfeld, *J. Electrochem. Soc.*, **143**, 587 (1996).
10. Y. Bultel, L. Genies, O. Antoine, P. Ozil, and R. Durand, *J. Electroanal. Chem.*, **527**, 143 (2002).
11. F. Jaouen and G. Lindbergh, *J. Electrochem. Soc.*, **150**, A1699 (2003).
12. Q. Guo and R. E. White, *J. Electrochem. Soc.*, **151**, E133 (2004).
13. Y. Bultel, K. Wiezell, F. Jaouen, P. Ozil, and G. Lindbergh, *Electrochimica Acta*, **51**, 474 (2005).
14. D. Gerteisen, A. Hakenjos, and J. O. Schumacher, *J. Power Sources*, **173**, 346 (2007).
15. A. A. Franco, P. Schott, C. Jallut, and B. Maschke, *Fuel Cells*, **7**, 99 (2007).
16. J. Deseure, *J. Power Sources*, **178**, 323 (2008).
17. M. Cimenti, D. Bessarabov, M. Tam, and J. Stumper, *ECS Transactions*, **28**, 147 (2010).
18. I. A. Schneider, M. H. Bayer, and S. von Dahlen, *J. Electrochem. Soc.*, **158**, B343 (2011).
19. J. Mainka et al., *Fuel Cells*, **12**, 848 (2012).
20. J. R. Vang, S. J. Andreasen, and S. K. Kaer, *J. Fuel Cell Sci. Techn.*, **9**, 021005 (2012).
21. O. Shamardina, M. S. Kondratenko, A. V. Chertovich, and A. A. Kulikovsky, *Int. J. Hydrogen Energy*, **39**, 2224 (2014).
22. B. P. Setzler and T. F. Fuller, *J. Electrochem. Soc.*, **162**, F519 (2015).
23. A. A. Kulikovsky and M. Eikerling, *J. Electroanal. Chem.*, **691**, 13 (2013).
24. R. de Levie, Electrochemical response of porous and rough electrodes, in *Advances in Electrochemistry and Electrochemical Engineering*, edited by P. Delahay, volume 6, pages 329–397, Interscience, New–York, 1967.
25. A. Lasia, *J. Electroanal. Chem.*, **397**, 27 (1995).
26. A. Lasia, *J. Electroanal. Chem.*, **428**, 155 (1997).
27. M. Eikerling and A. A. Kornyshev, *J. Electroanal. Chem.*, **475**, 107 (1999).
28. A. A. Kulikovsky, *Electrochimica Acta*, **147**, 773 (2014).
29. T. Reshetenko and A. Kulikovsky, *J. Electrochem. Soc.*, **162**, F627 (2015).
30. I. A. Schneider, S. A. Freunberger, D. Kramer, A. Wokaun, and G. G. Scherer, *J. Electrochem. Soc.*, **154**, B383 (2007).
31. I. A. Schneider, D. Kramer, A. Wokaun, and G. G. Scherer, *J. Electrochem. Soc.*, **154**, B770 (2007).
32. A. A. Kulikovsky, *J. Electrochem. Soc.*, **159**, F294 (2012).
33. T. V. Reshetenko, G. Bender, K. Bethune, and R. Rocheleau, *Electrochimica Acta*, **56**, 8700 (2011).
34. S. J. C. Cleghorn, C. R. Derouin, M. S. Wilson, and S. Gottesfeld, *J. Appl. Electrochem.*, **28**, 663 (1998).
35. J. Stumper, S. A. Campbell, D. P. Wilkinson, M. C. Johnson, and M. Davis, *Electrochimica Acta*, **43**, 3773 (1998).
36. G. Bender, M. S. Wilson, and T. A. Zawodzinski, *J. Power Sources*, **123**, 163 (2003).
37. C. Wieser, A. Helmbold, and E. Gulzow, *J. Appl. Electrochem.*, **30**, 803 (2000).
38. A. A. Kulikovsky, *Electrochimica Acta*, **49**, 617 (2004).
39. M. Keddam, C. Rakotomavo, and H. Takenouti, *J. Power Sources*, **161**, 920 (2006).
40. D. Malevich, E. Halliop, B. A. Peppley, J. G. Pharoah, and K. Karan, *J. Electrochem. Soc.*, **156**, B216 (2009).
41. R. Makharia, M. F. Mathias, and D. R. Baker, *J. Electrochem. Soc.*, **152**, A970 (2005).
42. P. Han and D. M. Bartels, *J. Chem. Phys.*, **100**, 5597 (1996).
43. K. Malek, T. Mashio, and M. Eikerling, *Electrocatal.*, **2**, 141 (2011).
44. J. Ihonen, F. Jaouen, G. Lindbergh, A. Lundblad, and G. Sundholm, *J. Electrochem. Soc.*, **149**, A448 (2002).
45. M. F. Mathias, J. Roth, J. Fleming, and W. Lehnert, Diffusion media materials and characterisation, in *Handbook of Fuel Cells: Fundamentals, Technology, Applications*, edited by W. Vielstich, A. Lamm, and H. A. Gasteiger, volume 3, pages 517–538, Wiley, New–York, 2003.
46. M. Uchida, Y. Aoyama, N. Eda, and A. Ohta, *J. Electrochem. Soc.*, **142**, 4143 (1995).
47. T. V. Reshetenko, H.-T. Kim, and H.-J. Kweon, *Electrochimica Acta*, **53**, 3043 (2008).
48. S. Park, J.-W. Lee, and B. N. Popov, *J. Power Sources*, **163**, 357 (2006).
49. M. Watanabe, M. Tomikawa, and S. Motoo, *J. Electroanal. Chem.*, **195**, 81 (1985).